PHYSICAL REVIEW ACCELERATORS AND BEAMS **25,** 121301 (2022)

# Design, fabrication, and tuning of a THz-driven electron gun

Samantha M. Lewis,* Julian Merrick, Mohamed A. K. Othman, Andrew Haase,
Sami Tantawi, and Emilio A. Nanni
*SLAC National Accelerator Laboratory, Menlo Park, California 94025, USA*

(Received 31 March 2022; accepted 18 November 2022; published 14 December 2022)

We present the design, fabrication, and cold testing of a THz-driven field emission electron gun. The gun is designed as a two-cell standing-wave structure with a copper tip inserted halfway into the first cell that serves as the field emission source. It is powered by a 110 GHz gyrotron and is expected to produce 51 fC, 360 keV electron bunches with an input power of 500 kW. Several gun structures were fabricated using a high precision diamond turned mandrel and copper electroforming. The frequencies of the cavity resonances were mechanically tuned using azimuthal compression.

DOI: 10.1103/PhysRevAccelBeams.25.121301

## I. INTRODUCTION

Next generation accelerator facilities require new electron source technology [1]. The properties of the electron source heavily influence the achievable beam parameters in applications such as free electron lasers (FELs) [2–4] and ultrafast electron diffraction (UED) [5–7]. Existing facilities have proven extremely useful for studying novel materials and fundamental biological and chemical processes. To access new regimes of study, these systems require improvements in emittance, bunch length, energy spread, brightness, and synchronization. There are a number of research efforts dedicated to providing electron sources and acceleration techniques to meet these requirements.

A significant area of research is focused on increasing the accelerating gradient, which can help prevent beam degradation and provide high brightness sources in a small footprint. To date, advances towards high gradient acceleration have been made using a variety of techniques. The leading technology is plasma wakefield acceleration (PWA), in which electrons are accelerated using wakes generated by a laser or particle beam [8–12]. These experiments have demonstrated multi-GeV/m gradients and produced GeV-scale beams using staged acceleration. However, plasma instabilities pose challenges to delivering the beam performance required for future facilities.

In traditional normal conducting radio-frequency (NCRF) accelerator structures, the achievable gradient is limited by the breakdown voltage [13]. The strength of the electric field in the cavity directly determines the accelerating gradient. Higher gradients require stronger electric fields, but vacuum breakdowns occur when the surface fields are too high. Experiments at various frequencies [14–16] have shown that the achievable surface electric field $E_s$ before breakdown increases with higher frequencies $f$ and shorter pulse lengths $\tau$. The achievable $E_s$ fundamentally limits the maximum possible gradient within commonly used NCRF cavities. A promising potential solution is developing similar accelerators at much higher frequencies. Experiments have been performed using dielectric-loaded THz waveguides to achieve gradients of 85 MeV/m [17]. Wakefield-driven traveling-wave structures have demonstrated gradients of 300 MeV/m [18], and standing wave structures have reached 230 MeV/m with limited input power [19].

Scaling accelerators to higher frequencies could provide performance benefits in addition to reaching higher gradients. Experiments have shown that breakdown behavior is influenced by the surface magnetic field and pulsed heating [20,21]. The timescale of pulsed heating is related to the pulse length $\tau$, which is in turn determined by the required fill time of the structure. High frequency standing-wave structures require a shorter fill time, given by

$$t_F = \frac{2Q_L}{\omega} = \frac{2Q_0}{(1+\beta_c)\omega}, \tag{1}$$

where $Q_L$ and $Q_0$ are the loaded and unloaded quality factors, $\beta_c$ is the coupling constant, and $\omega$ is the angular frequency. By reducing the required fill time and pulse length, pulsed heating can be reduced in high frequency cavities. Additionally, the shunt impedance scales as $f^{1/2}$ and the dissipated power per unit length scales as $f^{-1/2}$. These scalings could lead to lower losses and the ability to operate with high repetition rates.

---

[*] smlewis@fnal.gov

At the low end of the THz regime, it is possible to take advantage of frequency scaling improvements while still leveraging the extensive experience gained from operating traditional rf accelerators. Recent research efforts have made significant strides towards providing high power THz sources [22–25]. The small size of THz cavities poses fabrication challenges, but also opportunities to use advanced fabrication techniques. Significant efforts have been made to study the fabrication and performance of copper THz structures, paving the way for the development of a high gradient THz accelerator [26–28]. This includes studies of split-block copper structures that have explored bonding techniques capable of withstanding the high surface fields and providing the precision alignment needed for mm-scale cavities.

In addition to improvements from high gradient acceleration, there are performance requirements that necessitate new electron source technology. The quality of the electron source determines the achievable beam performance downstream. Generating and quickly accelerating short, low emittance electron bunches is fundamental to reaching new regimes of operation for both FEL and UED facilities. Electron source research efforts are underway to improve the performance of existing gun types as well as to develop new materials and techniques [29–35]. Electron guns can use a variety of emission mechanisms including thermionic, photo, and field emission [36–38]. In the case of field emission, the surface electric field on the tip lowers the potential barrier such that electrons can tunnel from the cathode material, generating a beam.

THz-frequency cavities developed for high gradient acceleration make ideal candidates for building compact field and photofield emission sources. Aside from providing high surface fields, a high acceleration gradient helps preserve the beam quality. Additionally, the fast timescale of the rf cycles in THz cavities naturally limits the bunch length.

To demonstrate this potential, we have designed and built a THz-based field emission electron gun. The gun is a two-cell standing-wave structure designed to operate at 110 GHz in the $\pi$ mode. We used the novel fabrication technique of electroforming to fabricate the cells and the copper tip used as the electron source. The use of electroforming allows for the cathode tip to be fabricated in one piece with the cells, which would not be possible with split block machining. This fabrication method also allowed us to tune the cavity frequencies into the ideal range required for our THz source. This represents the first demonstration of mechanical tuning of W-band accelerator cavities. This is also the first W-band accelerator structure made through electroforming.

In this paper, we present the design of the gun, cold tests, and details on our tuning procedure. Section II outlines the design and expected performance based on electromagnetic and particle beam simulations. Section III discusses the fabrication procedure, cold tests, and imaging used to characterize the structures. Section IV describes multiple attempts at tuning the guns and presents measurements of a structure after tuning.

## II. DESIGN AND MODELING

The electron gun is designed as a two-cell, standing-wave structure. In a standing-wave electron gun, the electromagnetic field is excited by an external rf source. The electric field on-axis accelerates the beam emitted from the cathode. The cell length and frequency are designed such that the phase advance between the cells gives consistent acceleration for a given electron beam energy. The mode of operation of this gun is the $\pi$ mode, which has a 180° shift for each cell.

A schematic and model of the gun structure are shown in Fig. 1. The design values of each parameter are summarized in Table I. A copper tip with a 50 μm radius serves as the field emission source. The electromagnetic performance of the gun cells was modeled using Ansys's high frequency structure simulator (HFSS) [39]. The structure was designed such that the electric field is strongest in the first cell, providing high surface fields on the tip. For an input power of 500 kW, the field on the tip was calculated to be 3.9 GV/m, which is roughly 4.5 times the highest surface electric field elsewhere in the structure.

The peak surface magnetic field occurs at the base of the tip and was calculated to be 1.4 MA/m for 500 kW of input power. A calculation of the pulsed heating was performed based on this peak value, giving a range of 100–130 °C depending on the gyrotron pulse parameters. The nominal length of the gyrotron pulse used in this calculation was 10 ns, which is similar to the pulses used in [19]. The gyrotron pulse length tunable used a laser-controlled semiconductor switch [40]. This pulsed heating value exceeds the thermal cyclic fatigue thresholds found in [21] and may be the limiting mechanism for the lifetime of the tip. In future iterations, the geometry of the tip could be optimized

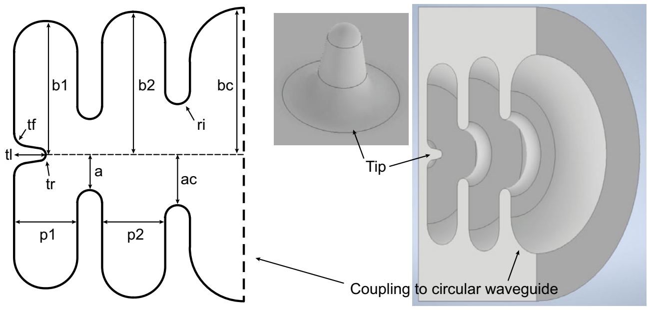

FIG. 1. Schematic and model of the copper tip gun. The structure is cylindrically symmetric around the horizontal dashed line shown. The structure consists of two cells, a copper tip (the cathode) located in the center of the first cell, and a coupling section. Input power is coupled in on-axis through a circular waveguide.

TABLE I. Design values of the copper tip gun.

| Parameter | Value (mm) | Description |
|---|---|---|
| a | 0.286 | Iris radius |
| ac | 0.408 | Coupling iris radius |
| b1 | 1.080 | Radius of first cell |
| b2 | 1.155 | Radius of second cell |
| bc | 1.185 | Radius of input circular waveguide |
| p1 | 0.51 | Length of first cell |
| p2 | 0.51 | Length of second cell |
| ri | 0.1 | Iris radius of curvature |
| tf | 0.1 | Tip base radius of curvature |
| tl | 0.255 | Tip length |
| tr | 0.050 | Tip radius of curvature |

to reduce the peak surface magnetic field. Elsewhere in the gun structure, the highest surface magnetic fields are a factor of 2 lower, giving heating on the order of 50 °C. This value is below the thermal cyclic fatigue threshold for copper and is consistent with previous mm-wave structure experiments [19].

The gun is powered by a 110 GHz megawatt gyrotron which has been used to study breakdown in copper W-band cavities [19]. The output beam from this gyrotron is transported in free space. To couple into the structure, the beam is focused onto a Gaussian horn which is followed by a mode converter to produce the $\mathrm{TM}_{01}$ circular waveguide mode. This circular waveguide section of the mode converter mates with the coupling section of the gun cells. Figure 2 shows the mode converter and the simulated fields of the $\pi$ mode in the structure. The Gaussian horn and mode converter performance has been established by previous breakdown experiments [19,41,42]. In this case, the mode converter wall has been modified to include a beam tunnel that does not affect the performance.

Particle simulations of the beam dynamics were performed using a general particle tracer (GPT) [43] combined with the HFSS fields and a Fowler-Nordheim-based model of the field emission. The Fowler-Nordheim equation describes cold field emission as a function of an applied electric field $E$ and a material-dependent work function $\phi$. The equation can be written as

$$I_F = \frac{1.54\times 10^{-6}\times 10^{4.52\phi^{-0.5}} A_e \beta^2 E^2}{\phi} \times \exp\left(-\frac{6.53\times 10^{9}\phi^{1.5}}{\beta E}\right)\ [\mathrm{A}] \tag{2}$$

with $E$ in units of V/m and $\phi$ in units of eV [44,45]. The current calculation is based on an area $A_e$ and a field enhancement factor $\beta$, which represents local field enhancement due to surface features. A simple model was developed to calculate the field-emitted bunch charge based on the simulated surface fields in HFSS. The copper tip was discretized using 10 points along the 50 μm radius. The field at each point was used to represent a ring of surface area on the tip hemisphere assuming azimuthal symmetry. The current $I$ of each of these rings was calculated based on the corresponding area. These points are shown in Fig. 3. The resulting current versus rf phase is shown in Fig. 4. The current density is highest at the center, which is expected based on the field distribution. The field at the outermost points is low enough such that the emitted current is effectively zero.

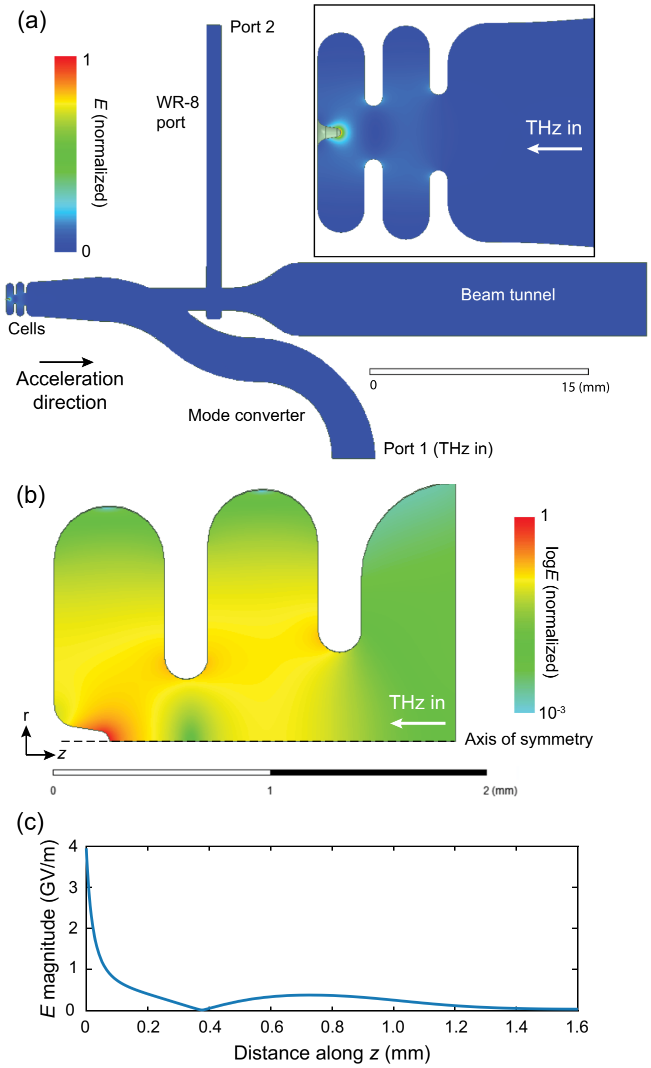

FIG. 2. (a) Electric field in the vacuum space of the mode converter and gun structure on the $\pi$ mode resonance. The simulation assumes mirror symmetry across the plane shown and uses copper surface resistivity for all external boundaries of the vacuum space excluding ports and the beam tunnel exit. The electric field is shown in normalized units. Power is input from port 1 and coupled into the cells. The inset shows the field profile in the cells including field enhancement at the tip. (b) Log-scale plot of the electric field in the cells, showing the field balance between the two cells. This simulation assumes cylindrical symmetry around the dashed line. (c) On-axis electric field magnitude for an input power of 500 kW.

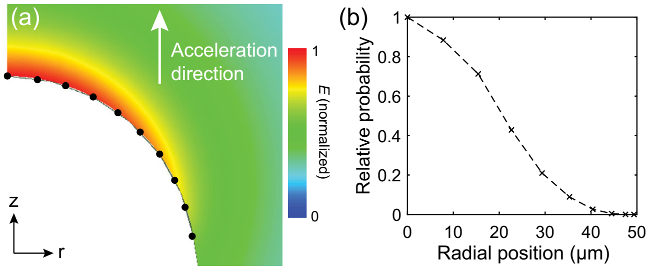

FIG. 3. (a) HFSS electric field on the tip showing the points which were used to discretize the emission area. (b) Relative probability of emission at those points based on the current density calculated from the Fowler-Nordheim equation.

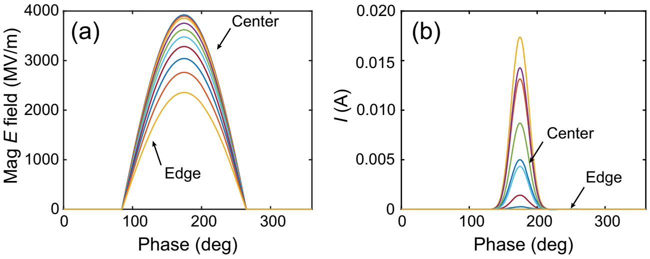

FIG. 4. (a) Magnitude of the electric field at the points shown in Fig. 3. Half of the rf cycle is shown which is the correct orientation for acceleration. (b) The current versus phase based on the fields in (a). Most emission comes from the center and surrounding area. While the field is highest at the center of the tip, the current is higher at some points because they represent a larger area in a high-field region. The current density is highest at the tip center where the field is highest. The field is low enough at the edge of the hemisphere that it does not significantly contribute to the emission. This is reflected in the radial probability shown in Fig. 3(b).

The total bunch charge emitted from the tip in one rf cycle (9 ps) was calculated to be 51 fC based on 500 kW of input power. This calculation assumed a value of $\phi = 4.7$ based on a range of possible values for different copper crystal structures and polycrystalline films [46–48]. The true work function of the copper tip may vary, especially given the tip is produced additively through electroforming. Additionally, no field enhancement factor $\beta$ was assumed. In reality, surface features will lead to additional local field enhancement. Thus, this calculation represents a minimum expected bunch charge per rf cycle for a smooth surface.

The structure has a fill time on the order of 10 ns before the full field is reached. During this time, the bunch charge will vary with increasing surface electric field until the field reaches its full value. Decreasing bunch charge will be seen after the pulse as power in the structure dissipates and the surface field decreases. A single gyrotron pulse will result in thousands of rf cycles and therefore thousands of bunches. The amount of time the peak bunch charge is emitted will depend on the length of the tunable gyrotron pulse, which determines the amount of time the cavity is at its full field. Further discussion of the gyrotron pulse length and cavity fill time can be found in [49].

To represent the emission in GPT, the total bunch charge was distributed in space and time based on the Fowler-Nordheim calculations. The current density versus radius was normalized and used to set the probability of the $x$-$y$ spatial distribution of the macroparticles on a 2D surface at $z = 0$. It was not possible to create at 3D surface of emission in GPT to fully represent the emission surface. The model assumed symmetry in angle and a uniform $2\pi$ sr distribution in phase space. The probability of emission versus time was based on the emission versus phase at the tip center. All particles were assumed to be born with $E_0 = 0.4$ eV. This value was chosen as a conservative estimate given the unknowns of the true material work function and properties of the electroformed copper. The estimate was based on values typically seen in photocathodes [50]. In reality, there will be some energy spread in the emitted electrons which is not captured in this model. The cumulative distribution of the emitted beam is shown in Fig. 5.

To model the beam acceleration, the GPT simulations used the full 3D complex electric and magnetic fields of the gun structure calculated in HFSS for 500 kW of input power. Space charge was included using a built-in 3D mesh-based routine [51]. The beam energy and phase space after acceleration and a drift are shown in Fig. 6. The maximum kinetic energy is 366 keV, corresponding to $\gamma = 1.717$. While the core of the bunch is accelerated, there is a low energy tail. Roughly 74% of the particles fall within 5% of the maximum energy, and 85% fall within 10% of $E_{\mathrm{max}}$. The normalized transverse rms emittance was calculated using the built-in GPT routine. The emittance for particles within 5% of the peak energy is $\epsilon_N = 0.88$ mm-mrad and for particles within 10% of the peak

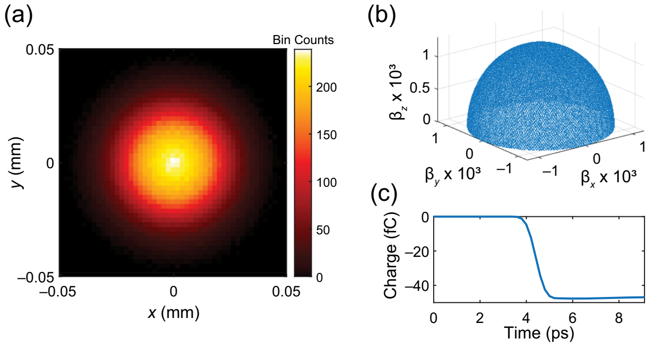

FIG. 5. Cumulative (a) spatial and (b) angular distribution of a beam. The radial distribution is set by the relative probability calculated using the HFSS fields on the tip. Emission is concentrated in the center and there is very little emission at the edges. (c) The build up of charge versus time based on the emission versus phase shown in Fig. 4. The maximum value is never completely reached because some particles are lost while others are being emitted. One rf cycle is shown.

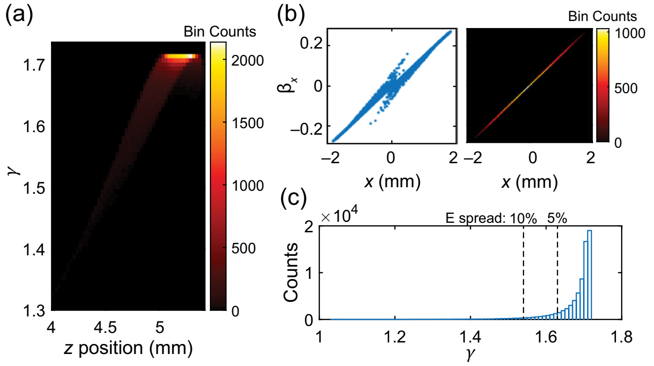

FIG. 6. (a) Longitudinal phase space after acceleration and a drift. The peak is highly localized near the maximum achievable energy. (b) Scatter and density plots of the transverse phase space after acceleration and a drift, showing the beam diverging. The beam is symmetric in $x$ and $y$ and thus only $x$-$\beta_x$ is shown. (c) Histogram of the electron energy distribution. The clear peak is at around $\gamma = 1.71$–$1.72$ or about 365 keV, very close to the single particle prediction. The energy bins are $\gamma = 0.01$ or roughly 5 keV. The dashed lines indicate the cutoffs for 5% and 10% energy spread from the maximum value.

it is $\epsilon_N = 1.04$ mm-mrad. These values are on par with existing photocathode values and are the expected order of magnitude for a 50 μm radius tip.

The accuracy of this calculation is limited by the 2D modeling of the emission surface. Due to the curvature of the tip, there will be a $z$ distribution of the emitted particles that is not captured in this model. However, Fig. 3(b) shows that few particles are emitted from the outer points on the tip and the majority of electrons are emitted close to the tip center. Additionally, a significant fraction of the off-axis particles are lost during acceleration because there is no focusing element around the cells. The emittance calculation and the distributions shown in Fig. 6 are based on the particles which survive acceleration and exit the cell structure. Details about the beam transport through the full gun focusing and detector assembly are beyond the scope of this paper, but additional discussion can be found in [49]. The emittance accuracy is also limited by the assumed constant value of the initial electron energy.

The GPT simulations included modeling of the full beam transport for high power testing. The nominal operating point for the design of the assembly was chosen to be 500 kW of input power, and simulations were performed to confirm that the gun could provide acceleration for input powers as low as 50 kW. Discussion of the design of the magnets and beam diagnostics for high power testing will be presented in a future paper.

## III. COLD TESTS AND CHARACTERIZATION

Multiple gun structures were fabricated via electroforming. First, the vacuum space of the cells and circular waveguide was machined into an aluminum mandrel using high precision diamond point turning. The tip portion was removed from the mandrel using sink electrical discharge machining (EDM). Copper was electroformed around the aluminum mandrel. Electroforming produces a copper bulk with an interior surface matching the dimensions of the aluminum mandrel, making it possible to create small complex features like the cathode tip. The outer surface of the copper was machined to produce a smooth cylinder. After this machining, the mandrel was dissolved using sodium hydroxide. The electroformed structure includes the cells, tip, and coupling section as one monolithic piece. Photos of one structure are shown in Fig. 7.

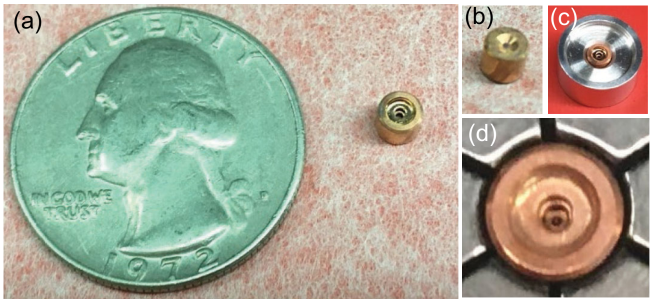

FIG. 7. Photos of the fabricated gun structures. (a) Cells with the coupling opening pointed up. The coupling iris and inner iris are both visible. (b) Back of the structure showing a divot for centering and alignment in the final assembly. (c) Cell structure upright in an aluminum adapter for cold testing. (d) Close-up photo where inner features are visible. The copper tip is visible in the center and the inner iris is also visible.

A laser confocal microscope was used to image each structure in detail. Images of several structures are shown in Fig. 8. The microscope was used to measure the 3D profile of the cathode tip. Example height data and 3D images are shown in Fig. 9. Overall the measured parameters of the fabricated structures match well with the design, with small variations across the different structures.

Cold tests were performed on all of the fabricated structures. In each case, the cavity resonances were lower than the design values of 109.22 and 110.01 GHz for the 0 and $\pi$ modes, respectively. The range of measured 0 mode frequencies was 108.17–108.54 GHz, and the $\pi$ mode frequencies ranged over 109.61–109.90 GHz. The relative strength of the two modes and the mode spacing also differed significantly from the design. A comparison is shown in Fig. 10 with a representative measurement.

Additional modeling was performed to determine potential causes of the variation and investigate the resulting impact on the electron beam. The frequency shifts could not be explained by the structure being uniformly oversized. Instead, the simulations showed that there is a difference in the fabrication error of the radii of the two cells (b1 and b2), altering the field balance. Based on measurements of the mandrels before electroforming, it is also likely that there was an error in the length of the first cell. The full details of

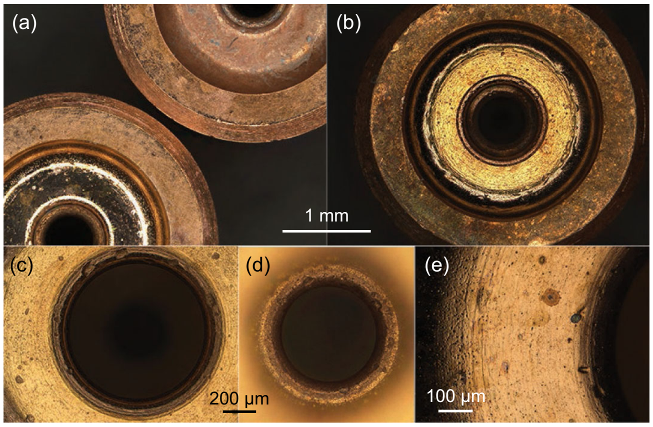

FIG. 8. Microscope images of different gun structures. All of the images are stacked focus images. (a) Side-by-side comparison of two structures showing the different surface finishes. (b) Image of a structure showing both irises and the input coupling section. The surface finish on the outer surface which mates with the input waveguide shows more wear and tear than the cell surfaces. (c) Close-up view of the coupling iris. There are pits visible in the iris. These features will likely be smoothed during high power processing. (d) The inner iris, viewed with the same magnification as (c). (e) Close-up view of the coupling iris edge and surface of the coupling cell.

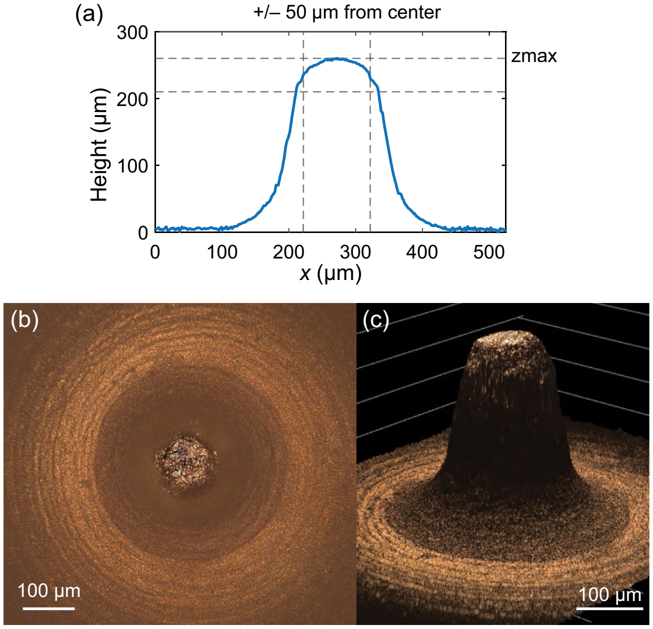

FIG. 9. (a) Height profile through the center of a copper tip. The dashed lines indicate the height and the distance corresponding to a 50 μm radius, the design value. The tip is not a perfect hemisphere, but its overall size matches well with the design. The height from the baseline is 255 μm, which was the design value for the height. (b) Top-down view of a tip in a stacked-focus image. (c) Height data displayed in 3D form.

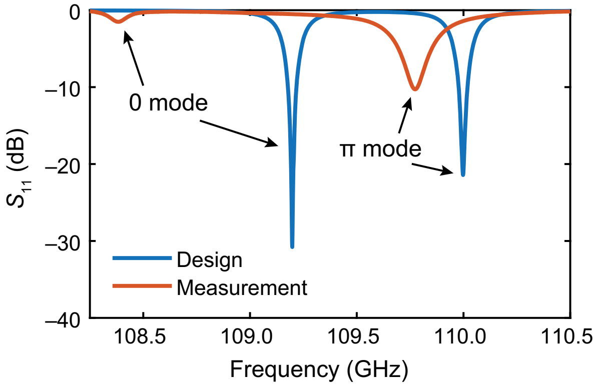

FIG. 10. An example measurement of the reflection signal ($S_{11}$) compared to the design. The 0 mode and $\pi$ mode are indicated. In the fabricated structures, both modes are lower in frequency than the design. There is also a clear difference in the relative strength of the two modes and their spacing.

this study are beyond the scope of this paper but can be found in [49]. The frequency shifts can be explained by deviations in these dimensions in the range of 1–10 μm.

## IV. TUNING

The operational tuning range of the gyrotron source is 110.08–110.12 GHz, with recent peak performance between 110.10 and 110.12 GHz. The $\pi$ mode did not fall within this range in any of the structures, making it necessary to tune the cells. Further, HFSS simulations matching the measured spectrum had a weaker electric field in the first cell and a stronger field in the second cell. GPT simulations based on these fields showed that the structure would still provide acceleration with a lower maximum energy. The reduced field in the first cell would also significantly lower the field on the tip, limiting the achievable bunch charge. Several methods of tuning were attempted to raise the frequency and correct the field balance. Active thermal tuning alone would be insufficient to bring the frequency within range for high power operation. Instead, a combination of chemical etching and mechanical tuning was required. Etching using HCl acid raised the frequency of both modes in all of the structures that were etched. This indicates there was some residual material—potentially aluminum from the mandrel—that affected the frequency.

Following etching, several structures were mechanically tuned using a ER collet to achieve azimuthal compression. Photos of a gun structure in the collet during tuning are shown in Fig. 11. The orientation of the structure in the collet affected the degree of tuning of the two modes. Using a careful series of small tuning steps, it was possible to tune the 0 mode by a larger shift than the $\pi$ mode. The resulting spectrum matches more closely with the original design. Additional modeling was performed to match the measurements after tuning. These simulations indicate the field

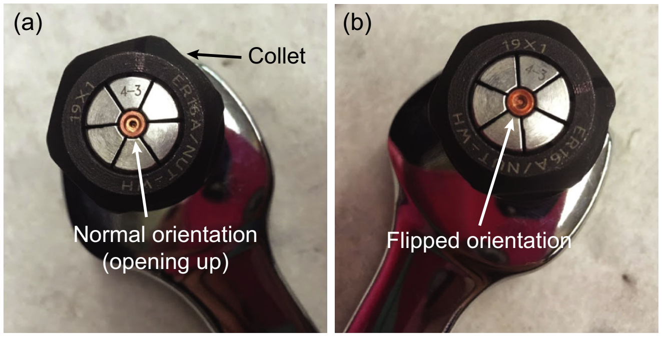

FIG. 11. Images of a structure in the tuning collet. (a) The "normal" orientation with the circular input waveguide opening pointing up. The circular waveguide opening is indicated in Fig. 1. A close-up view of the gun in this position is shown in Fig. 7(d). (b) The "flipped" orientation with the input waveguide pointing down into the collet and the divot on the back of the structure shown [see Fig. 7(b)].

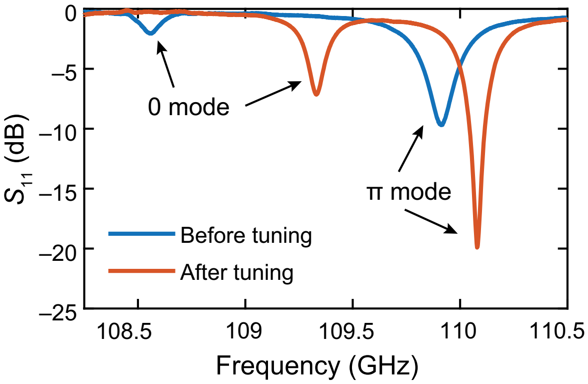

FIG. 12. The measured reflection $S_{11}$ before and after tuning. The 0 mode and $\pi$ mode are indicated. The 0 mode was intentionally tuned by a larger degree than the $\pi$ mode in order to achieve better field balance for acceleration and emission.

balance and surface field on the tip should provide significantly better performance than the structures as fabricated. The measured $S_{11}$ of the final structure before and after mechanical tuning is shown in Fig. 12. The final frequency of the $\pi$ mode was 110.081 GHz. Measurements under vacuum showed a shift to the expected value of roughly 110.114 GHz, which was measured in multiple air to vacuum cycles. This is within the current operating range of the gyrotron source. Additional fine-tuning to raise or lower the frequency can be performed thermally, achieving a change of roughly 1.6 MHz per °C. The full gun assembly includes a cooling assembly to utilize thermal fine-tuning if necessary [49].

## V. SUMMARY AND FUTURE WORK

We have developed a field emission electron gun at 110 GHz and demonstrated the feasibility of fabricating high frequency accelerator structures using electroforming. Images of the structures showed a high degree of accuracy to the design. Small deviations on the order of 1–10 μm were able to be corrected using etching and mechanical tuning. This is the first demonstration of mechanical tuning of a W-band accelerator structure.

In our fabricated gun structures, the errors in dimensions were larger than the design, resulting in lower frequencies that needed to be tuned higher. The compression method worked to raise the frequencies, but this method could not have been used to lower the frequencies if the structures had been smaller than designed. Because the copper is electroformed around a mandrel, the dimensions of the final structure will be limited by the mandrel size. Thus, it is practical to err on the side of a slightly oversized mandrel to ensure the structures are not made with frequencies that are too high. Thermal tuning can be used to slightly tune the frequencies in either direction when the frequency difference is small.

The gun cells are part of a larger assembly which will be used to characterize the beam during high power testing. The gun will be operated at room temperature and is expected to produce 51 fC, 360 keV electron bunches with 500 kW of input power. In addition to measuring the energy spread, beam size, and field-emitted current, the high power measurements will include breakdown monitoring and build on previous W-band breakdown studies. Details on the assembly and beam characterization setup can be found in [49]. The results of the high power measurements will be reported in a future paper. The gun is capable of providing acceleration over a range of input powers and thus the emission properties of the cathode will be examined at multiple operating points. The gun cells are fully demountable from the rest of the assembly and multiple structures have been tuned within the gyrotron's operational range. This will provide the opportunity to study the efficacy of different tuning methods and provide confirmation of the effects of the mode balance on acceleration and emission.

Future work will include a structure with multiple stages of W-band acceleration following the gun to develop a THz-driven, normal conducting linac. This gun was designed for energies and bunch charges that are most applicable to UED experiments. Successive acceleration stages could be used to bring the beam to higher energies for FEL or collider applications. Other cathode materials and types will also be explored, including the use of diamond field emitter arrays (DFEAs) and photofield sources [49,52,53]. Photofield sources and different tip geometries could greatly improve the emittance.

## ACKNOWLEDGMENTS

We gratefully acknowledge Dale Miller, Andy Nguyen, Mario Cardoso, Walter Brown, and the SLAC TID Advanced Prototyping and Fabrication team for their assistance with structure fabrication. We would like to thank Dennis Palmer for his assistance with rf measurements and Emma Snively for her help with GPT simulations. We also thank our colleagues Julian Picard, Elliot Claveau, Samuel Schaub, and Richard Temkin for valuable discussions about the gyrotron source and high power testing. This work was supported by the Department of Energy Contract No. DE-AC02-76SF00515 (SLAC) and by NSF Grant No. PHY-1734015.

[1] E. Lessner, X. Wang, and P. Musumeci, Report of the basic energy sciences workshop on the future of electron sources, Department of Energy, Washington, DC, 2016, 10.2172/1616511.

[2] D. A. G. Deacon, L. R. Elias, J. M. J. Madey, G. J. Ramian, H. A. Schwettman, and T. I. Smith, First Operation of a Free-Electron Laser, Phys. Rev. Lett. **38**, 892 (1977).

[3] P. Emma *et al.*, First lasing and operation of an ångstrom-wavelength free-electron laser, Nat. Photonics **4**, 641 (2010).

[4] K. Tiedtke *et al.*, The soft x-ray free-electron laser FLASH at DESY: Beamlines, diagnostics and end-stations, New J. Phys. **11**, 023029 (2009).

[5] A. H. Zewail, 4D ultrafast electron diffraction, crystallography, and microscopy, Annu. Rev. Phys. Chem. **57**, 65 (2006).

[6] R. Srinivasan, V. Lobastov, C.-Y. Ruan, and A. Zewail, Ultrafast electron diffraction (UED), Helv. Chim. Acta **86**, 1761 (2003).

[7] S. P. Weathersby *et al.*, Mega-electron-volt ultrafast electron diffraction at SLAC National Accelerator Laboratory, Rev. Sci. Instrum. **86**, 073702 (2015).

[8] B. Hidding, B. Foster, M. J. Hogan, P. Muggli, and J. B. Rosenzweig, Directions in plasma wakefield acceleration, Philos. Trans. R. Soc. A **377**, 20190215 (2019).

[9] E. Gschwendtner and P. Muggli, Plasma wakefield accelerators, Nat. Rev. Phys. **1**, 246 (2019).

[10] C. Joshi *et al.*, Plasma wakefield acceleration experiments at FACET II, Plasma Phys. Controlled Fusion **60**, 034001 (2018).

[11] C. Jing *et al.*, Electron acceleration through two successive electron beam driven wakefield acceleration stages, Nucl. Instrum. Methods Phys. Res., Sect. A **898**, 72 (2018).

[12] I. Blumenfeld *et al.*, Energy doubling of 42 GeV electrons in a metre-scale plasma wakefield accelerator, Nature (London) **445**, 741 (2007).

[13] W. D. Kilpatrick, Criterion for vacuum sparking designed to include both rf and dc, Rev. Sci. Instrum. **28**, 824 (1957).

[14] C. Limborg-Deprey, C. Adolphsen, D. McCormick, M. Dunning, K. Jobe, H. Li, T. Raubenheimer, A. Vrielink, T. Vecchione, F. Wang, and S. Weathersby, Performance of a first generation x-band photoelectron rf gun, Phys. Rev. Accel. Beams **19**, 053401 (2016).

[15] R. Akre *et al.*, Commissioning the Linac Coherent Light Source injector, Phys. Rev. ST Accel. Beams **11**, 030703 (2008).

[16] W. J. Brown, S. Trotz, K. Kreischer, M. Pedrozzi, M. Shapiro, and R. Temkin, Experimental and theoretical investigations of a 17-GHz rf gun, Nucl. Instrum. Methods Phys. Res., Sect. A **425**, 441 (1999).

[17] H. Xu, L. Yan, Y. Du, W. Huang, Q. Tian, R. Li, Y. Liang, S. Gu, J. Shi, and C. Tang, Cascaded high-gradient terahertz-driven acceleration of relativistic electron beams, Nat. Photonics **15**, 426 (2021).

[18] M. Dal Forno, V. Dolgashev, G. Bowden, C. Clarke, M. Hogan, D. McCormick, A. Novokhatski, B. Spataro, S. Weathersby, and S. G. Tantawi, rf breakdown tests of mm-wave metallic accelerating structures, Phys. Rev. Accel. Beams **19**, 011301 (2016).

[19] M. A. K. Othman, J. Picard, S. Schaub, V. A. Dolgashev, S. M. Lewis, J. Neilson, A. Haase, S. Jawla, B. Spataro, R. J. Temkin, S. Tantawi, and E. A. Nanni, Experimental demonstration of externally driven millimeter-wave particle accelerator structure, Appl. Phys. Lett. **117**, 073502 (2020).

[20] V. Dolgashev, S. Tantawi, Y. Higashi, and B. Spataro, Geometric dependence of radio-frequency breakdown in normal conducting accelerating structures, Appl. Phys. Lett. **97**, 171501 (2010).

[21] L. Laurent, S. Tantawi, V. Dolgashev, C. Nantista, Y. Higashi, M. Aicheler, S. Heikkinen, and W. Wuensch, Experimental study of rf pulsed heating, Phys. Rev. ST Accel. Beams **14**, 041001 (2011).

[22] Z. Zhang *et al.*, A high-power, high-repetition-rate THz source for pump-probe experiments at Linac Coherent Light Source II, J. Synchrotron Radiat. **27**, 890 (2020).

[23] J. Schmerge *et al.*, A tunable, linac based, intense, broad-band THz source for pump-probe experiments, SLAC National Accelerator Laboratory, Menlo Park, CA, Technical Report No. SLAC-R-1049, 2015

[24] W. R. Huang, S.-W. Huang, E. Granados, K. Ravi, K.-H. Hong, L. E. Zapata, and F. X. Kärtner, Highly efficient terahertz pulse generation by optical rectification in stoichiometric and cryo-cooled congruent lithium niobate, J. Mod. Opt. **62**, 1486 (2015).

[25] K. Zhong, W. Shi, D. Xu, P. Liu, Y. Wang, J. Mei, C. Yan, S. Fu, and J. Yao, Optically pumped terahertz sources, Sci. China Technol. Sci. **60**, 1801 (2017).

[26] S. M. Lewis, E. A. Nanni, and R. J. Temkin, Direct machining of low-loss THz waveguide components with an rf choke, IEEE Microwave Wireless Compon. Lett. **24**, 842 (2014).

[27] E. A. Nanni, V. A. Dolgashev, A. Haase, J. Neilson, S. Tantawi, S. C. Schaub, R. J. Temkin, and B. Spataro, Prototyping high-gradient mm-wave accelerating structures, J. Phys. Conf. Ser. **874**, 012039 (2017).

[28] M. Othman, B. Angier, A. Haase, E. Nanni, M. Roux, and A. Sy, Prototyping of brazed mm-wave accelerating structures, in *Proceedings of the 10th International Particle Accelerator Conference, IPAC-2019, Melbourne, Australia* (JACoW, Geneva, Switzerland, 2019).

[29] C. M. Pierce, M. B. Andorf, E. Lu, C. Gulliford, I. V. Bazarov, J. M. Maxson, M. Gordon, Y.-K. Kim, N. P. Norvell, B. M. Dunham, and T. O. Raubenheimer, Low intrinsic emittance in modern photoinjector brightness, Phys. Rev. Accel. Beams **23**, 070101 (2020).

[30] L. Velardi, V. Turco, L. Monteduro, G. Cicala, A. Valentini, and V. Nassisi, Electron beams produced by innovative

photocathodes based on nanodiamond layers, Phys. Rev. Accel. Beams **22**, 093402 (2019).

[31] J. McCarter, Photocathode research for electron accelerators, Ph.D. thesis, University of Virginia, 2011.

[32] K. E. Nichols *et al.*, Demonstration of transport of a patterned electron beam produced by diamond pyramid cathode in an rf gun, Appl. Phys. Lett. **116**, 023502 (2020).

[33] L. Wimmer, G. Herink, D. R. Solli, S. V. Yalunin, K. E. Echternkamp, and C. Ropers, Terahertz control of nanotip photoemission, Nat. Phys. **10**, 432 (2014).

[34] S. Li and R. R. Jones, High-energy electron emission from metallic nano-tips driven by intense single-cycle terahertz pulses, Nat. Commun. **7**, 13405 (2016).

[35] X. Shao, A. Srinivasan, W. K. Ang, and A. Khursheed, A high-brightness large-diameter graphene coated point cathode field emission electron source, Nat. Commun. **9**, 1288 (2018).

[36] T. Asaka, T. Inagaki, T. Magome, N. Nishimori, Y. Otake, T. Taniuchi, K. Yanagida, and H. Tanaka, Low-emittance radio-frequency electron gun using a gridded thermionic cathode, Phys. Rev. Accel. Beams **23**, 063401 (2020).

[37] I. Petrushina *et al.*, High-Brightness Continuous-Wave Electron Beams from Superconducting Radio-Frequency Photoemission Gun, Phys. Rev. Lett. **124**, 244801 (2020).

[38] L. Zhou, H. Zha, J. Shi, J. Qiu, C. Wang, X. Lin, F. Liu, J. Gao, and H. Chen, Development of a high-gradient x-band rf gun with replaceable field emission cathodes for rf breakdown studies, Nucl. Instrum. Methods Phys. Res., Sect. A **1027**, 166206 (2022).

[39] Ansys, Ansys HFSS: High Frequency Electromagnetic Field Simulation, https://www.ansys.com/products/electronics/ansys-hfss.

[40] J. F. Picard, S. C. Schaub, G. Rosenzweig, J. C. Stephens, M. A. Shapiro, and R. J. Temkin, Laser-driven semiconductor switch for generating nanosecond pulses from a megawatt gyrotron, Appl. Phys. Lett. **114**, 164102 (2019).

[41] E. A. Nanni, M. D. Forno, V. A. Dolgashev, J. Neilson, and S. G. Tantawi, mm-wave standing-wave accelerating structures for high-gradient tests, in *Proceedings of the 7th International Particle Accelerator Conference, IPAC-2018, Busan, Korea* (JACoW, Geneva, Switzerland, 2016).

[42] E. Nanni, V. Dolgashev, A. Haase, S. Jawla, J. Neilson, S. Schaub, B. Spataro, S. Tantawi, and R. Temkin, Toward high-power high-gradient testing of mm-wave standing-wave accelerating structures, in *Proceedings of the 9th International Particle Accelerator Conference, IPAC-2018, Alexandria, Virginia* (JACoW, Geneva, Switzerland, 2018).

[43] S. B. van der Greer and M. J. de Loos, General Particle Tracer, http://www.pulsar.nl/gpt/.

[44] R. H. Fowler and L. Nordheim, Electron emission in intense electric fields, Proc. R. Soc. A **119**, 173 (1928).

[45] J. W. Wang, RF properties of periodic accelerating structures for linear colliders, Ph.D. thesis, Stanford University, 1989.

[46] *CRC Handbook of Chemistry and Physics*, 95th ed., edited by W. M. Haynes, D. R. Lide, and T. J. Bruno (CRC Press, Boca Raton, FL, 2014).

[47] J. Vancea, G. Reiss, D. Butz, and H. Hoffmann, Thickness-dependent effects in the work function of polycrystalline Cu-films, Europhys. Lett. **9**, 379 (1989).

[48] T. J. Drummond, Work functions of the transition metals and metal silicides, Report No. SAND99-0391J, 1999, https://www.osti.gov/biblio/3597.

[49] S. M. Lewis, A THz-driven electron gun, Ph.D. thesis, University of California, Berkeley, 2020.

[50] D. H. Dowell and J. F. Schmerge, Quantum efficiency and thermal emittance of metal photocathodes, Phys. Rev. ST Accel. Beams **12**, 074201 (2009).

[51] S. B. van der Greer and M. J. de Loos, General Particle Tracer user manual version 3.43 (section IV.8.1).

[52] E. I. Simakov, H. L. Andrews, M. J. Herman, K. M. Hubbard, and E. Weis, Diamond field emitter array cathodes and possibilities of employing additive manufacturing for dielectric laser accelerating structures, AIP Conf. Proc. **1812**, 060010 (2017).

[53] S. M. Lewis, V. Dolgashev, A. Haase, E. A. Nanni, M. Othman, A. Sy, and S. Tantawi, Design of a high-gradient THz-driven electron gun, *Proceedings of the 10th International Particle Accelerator Conference, IPAC-2019, Melbourne, Australia* (JACoW, Geneva, Switzerland, 2019).